Journal of
Materials Chemistry A

ROYAL SOCIETY
OF CHEMISTRY

PAPER

View Article Online
View Journal | View Issue

Check for updates

Cite this: *J. Mater. Chem. A*, 2023, **11**, 10699

Hydrogen bond-mediated pH-universal electrocatalytic hydrogen production by conjugated porous poly-indigo†

Ipsita Nath,[ab] Jeet Chakraborty,*[ab] Reinaud Lips,[ac] Sander Dekyvere,[a] Jiang Min,[a] Rajender S. Varma[d] and Francis Verpoort*[ae]

Received 26th October 2022
Accepted 19th April 2023

DOI: 10.1039/d2ta08365e

rsc.li/materials-a

High-performing catalysts for the hydrogen evolution reaction (HER) *via* water electrolysis are of great importance for producing carbon-free green fuels. Compared to the routinely used metal-based systems under acidic conditions, metal-free pH-universal HER catalysts are smarter options taking into account the practical usability, sustainability, biocompatibility, and nominal cytotoxicity. Herein, we present an indigo-based organic conjugated porous polymer featuring a pronounced 2D few-layered morphology with surface-decorated hydrogen bonding sites for a deep catalyst–water contact and promising electrochemical HER activity. Indigo, being a vat dye, reduces *in situ* to its anionic leuco analogue and further promotes catalytic activity. The material manifested equipotent activity in acidic, alkaline, and neutral media superior to the contemporary metal-free carbonaceous electrocatalysts and comparable to the state-of-the-art metal-based catalytic systems. Under appropriate conditions, the material showed an overpotential of only 28 mV at 10 mA cm^{-2} current density.

1. Introduction

Economic hydrogen production *via* water electrolysis is a long-standing scientific goal and has garnered substantial industrial traction to achieve climate goals.[1,2] To date, mostly various transition metals, platinum group metals and/or composites are used as catalysts for this purpose.[3–6] One specific drawback of these approaches is, indeed, their metal reliance. Citing the scarcity and cost of typical noble metals,[7] many "earth-abundant" metals/composites have been introduced as alternate catalysts instead.[8–12] Despite relative availability, a gradual increase in their price has been observed over the past few decades due to the augmented consumption of these metals in the electronics, chemical, and construction industries.[13] Once exhausted, their mitigated reproduction often leads to dampening of the material undermining the sustainability issue and ecological toxicity.[14–16] This, in turn, increases the production cost of the subsequent fresh batch of metals as their non-renewable resources continue to deplete. Moreover, the majority of these metal catalysts are pH-sensitive and show constrained activity in alkaline or neutral water.[17]

Heterogeneous organic semiconductors posit tangible potential in this regard as metal-free energy carriers.[18] One such genre of organic networks, called conjugated porous polymers (CPPs), has recently emerged as a metal-alternative catalyst for the photochemical HER.[19,20] CPPs are π-conjugated organic matrices possessing a superior surface area and permanent nano-porosity.[21–24] Their structural robustness makes them exceedingly stable over a wide pH range as well. However, the intrinsic hydrophobicity of the all-organic skeleton restrained their application in the electrochemical HER. The diminished contact between water and CPP leads to the generation of multiple air pockets that hamper electron flow resulting in a poor electrocatalytic activity.[18,19] The design of a CPP material amenable to circumvent these limitations under pH-universal conditions is yet to be described.

Earlier investigations have corroborated that surface texturing and incorporation of aqua-dissociable moieties can enhance the HER performance of metallic catalysts.[7,25–27] While water-dissociable moieties manifest ionic interactions with water molecules facilitating their dissociation, surface texturing creates rough edges, corners, and grain boundaries at the electrode surface thus boosting deep water–catalyst contact.[28] An analogous strategy can be adapted for CPP as well. The amorphous CPP particles are inherently grainy and extensively

---

[a] *State Key Laboratory of Advanced Technology for Materials Synthesis and Processing, Center for Chemical and Material Engineering, Wuhan University of Technology, Wuhan 430070, P.R. China. E-mail: jeet.chakraborty@hotmail.com; francis@whut.edu.cn*

[b] *Department of Chemistry, Ghent University, Krijgslaan 281, Ghent, 9000, Belgium*

[c] *Odisee Technologiecampus Gent, Ghent, 9000, Belgium*

[d] *Regional Centre of Advanced Technologies and Materials, Czech Advanced Technology and Research Institute, Palacký University in Olomouc, Šlechtitelů 27, 783 71 Olomouc, Czech Republic*

[e] *National Research Tomsk Polytechnic University, Lenin Avenue 30, Tomsk 634050, Russia*

† Electronic supplementary information (ESI) available. See DOI: https://doi.org/10.1039/d2ta08365e

porous. While this satisfies the requirement of surface texturing, water-interacting functionalities can be introduced using suitable organic struts. Additionally, a layered morphology of the material is preferred for enhanced conductivity and electron migration,[20] as well as for creating multiple water binding sites.

Indigo, a blue dye with rich historical significance,[29,30] comes in as a perfect fit in this scenario. The indigo family belongs to the domain of vat-dyes comprising hydrogen bond (H-bond) donating and accepting functionalities (Fig. S1†), which indicates its ability to generate an ionic structure in acidic and alkaline media through protonation–deprotonation, as well as maintaining van der Waals' interaction with water through H-bonding.[31–34] Moreover, they possess very low reduction potential suggesting their feasibility to catalyse the HER under low energy demanding conditions. With these thoughts in mind, we herein report an indigo-based CPP (Ind-CPP) as a metal-free HER catalyst that performs in pH-universal media with activity comparable to state-of-the-art catalytic systems.

Specifically, the chemical structure of indigo comprising a pair of carbonyl and amine units at ‘bay positions’ presents three possible sets of H-bonding interactions with water: $R_2C{=}O\cdots H{-}OH$, $H{-}R_2N\cdots H{-}OH$, and $R_2N{-}H\cdots OH_2$. Apart from these non-covalent attractions, each indigo protonates in an acidic medium ($R_2CO^+{-}H$ and $R_2HN^+{-}H$) enforcing the initial Volmer step of the HER. Alternatively, the reduced leuco indigo (*i.e.*, $[\mathrm{IndigoH}]^-$ or $[\mathrm{Indigo}]^{2-}$) interacts with water through electrostatic attraction (a property of vat-dyes) thus enhancing the rate of the Volmer reaction under neutral and alkaline conditions.[34] Due to these molecular-level interactions, the metal-free Ind-CPP inflicts deep water proximity while retaining its robust backbone and exhibits high HER performance with an overpotential of only 28 mV at a current density of 10 mA cm^{-2} under optimal conditions.

2. Results and discussion

2.1. Synthesis, characterization and properties

The general synthetic routes to CPPs are kinetically driven, producing amorphous particles of arbitrary size and morphology. However, contriving constrained diffusion of the reactants in the reaction media has been an empirically proven approach to delivering morphologically pronounced CPPs.[35,36] Seeking a similar procedure for Ind-CPP, we envisioned and designed 6,6′-dibromoindigo (Tyrian purple) and 1,3,5-triethynylbenzene as struts for the follow-up Sonogashira polymerization reaction. The 2D lamellar crystals of Tyrian purple are intrinsically insoluble in almost every solvent due to the strong intra- and inter-planner H-bonding at its molecular level and exhibit sparing solubility in DMF (Fig. S1, Discussion S1†).[32,33] We sought this opportunity and used DMF as the reaction solvent for Ind-CPP synthesis. The sparing solubility of Tyrian purple coerced the oligomeric intermediates obtained during CPP synthesis to arrange in a stable planner conformation (using H-bonding and π-stacking interactions) producing a morphologically pronounced 2D layered array of a deep bottle-green coloured polymer at the cost of a slower network propagation rate (Fig. S2†). The consideration behind our synthetic approach is vividly discussed in the ESI (Discussion S2).†

The FESEM image validates the stacked 2D sheet-type morphology of the as-synthesized Ind-CPP with surface dimensions ranging up to a few micrometres (Fig. 1a and S3†). The material can be visualized as stacked Lego layers where the H-bonding sites of the indigo moieties served as the *de facto* studs/binder units between two successive layers (Fig. 1d–f). The CPP, when subjected to ultrasonication in ethanol, appeared as few-layer lamellar sheets in the TEM image (Fig. 1b and S4†). The layered appearance of the material can be perceived from the 3D height profile diagram (Fig. 1c) of the selected area of the TEM image (red box, Fig. 1b). The embedded image-data histogram numerically promotes the layered growth of the organic network, wherein each layer with a corresponding apex in the histogram can be observed. This observation is indicative of a sonolysis-induced exfoliation of the inter-planner H-bonds of CPP into a few layers (Discussion S3†).[37,38] The exfoliated sheets provide an augmented catalyst–substrate contact leading to superior catalytic activity (Fig. S5, Discussion S4†). On the other hand, the amorphous nature of the polymer can be established from the diffused ring pattern of the selected area electron diffusion analysis (Fig. 1a, inset), as well as from the broad peak at *ca.* 20° in X-ray diffraction (XRD), characteristic of the long-range structural disorder present in amorphous materials (Fig. S6†).

The formation of the desired Ind-CPP structure can be confirmed from solid-state ^{13}C-NMR spectra (Fig. S7†). The typical peaks for sp-hybridized alkyne carbons appeared at 92.5 ppm confirming that ethynyl ends are connected to aromatic sidechains. The absence of any peak at *ca.* 80–82 ppm, where unreacted terminal alkynes typically appear, confirmed that 1,3,5-triethynyl benzene reacted completely with Tyrian purple. On the other hand, two characteristic signals were observed at 187.7 and 153.6 ppm arising from the carbonyl and the phenylic carbon adjacent to the N atom, respectively. The strong electronegativity of the neighbouring O and N can justify these down-field peaks. Another structure-specific signal originates at 110.8 ppm from the phenylic carbon α-to the carbonyl carbon. These three peaks conjointly confirm the presence of the indigo unit in the CPP, while the initial $-C{\equiv}C-$ signal inferred successful polymerization. Apart from these, other aromatic and central olefinic carbons provided superimposed signals over the central broad aromatic region.

The FTIR spectra further support this synthesis. The IR bands originating from the stretching of N–H and C=O, the key functionalities of indigo, emerged at *ca.* 3200 and 1600 cm^{-1}, respectively (Fig. S8 and Table S1†). On the other hand, the aromatic C=C and C–H stretching can also be observed at *ca.* 1560–1620 and 3050 cm^{-1}, respectively. Theoretical modelling of Ind-CPP shows two types of H-bonded structures (Fig. 1d–f). In the first case, HBD_{112}, the C=O of indigo is experiencing H-bonding with N–H of the same unit as well as with another one from the adjacent layer (Fig. 1e and S9†), whereas the interplanar interaction is absent in the second case (HBD_{11}, Fig. 1f and S9†). The H-bonding distances can be calculated to be 2.275

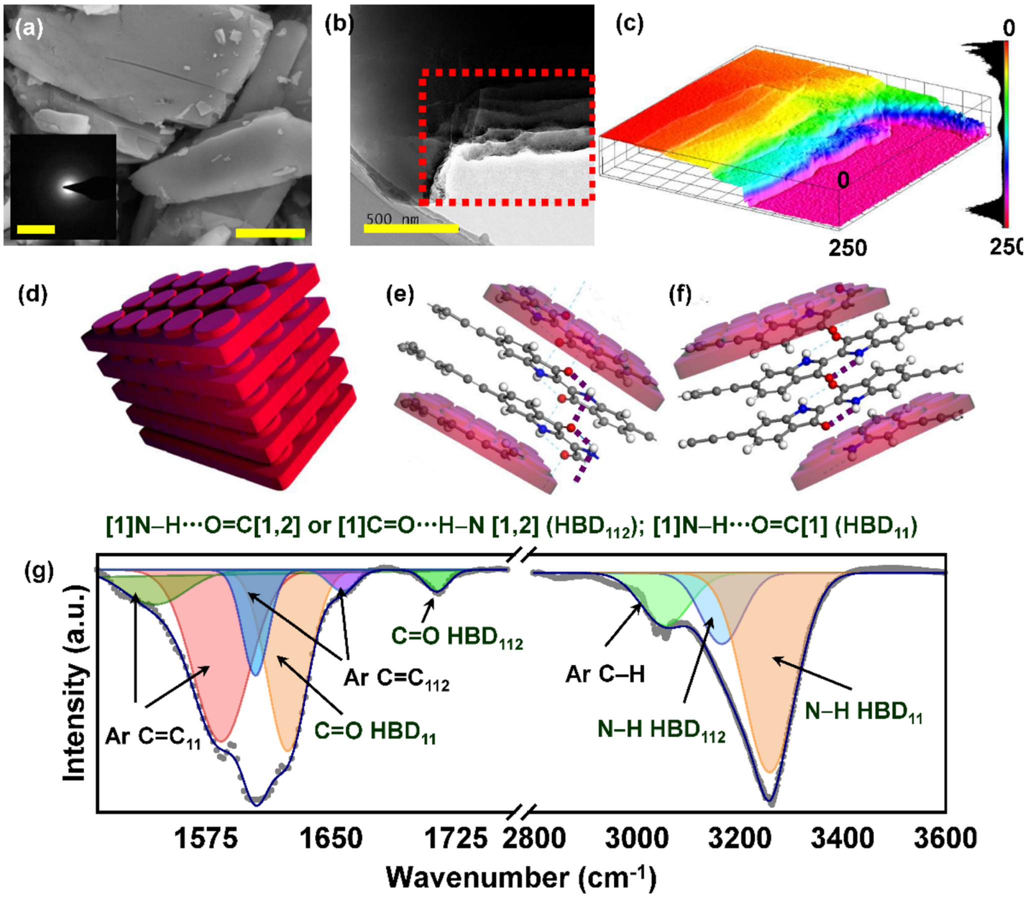

Fig. 1 (a) The FESEM image along with the SAED pattern (inset), scale bar 1 μm and 1/10 nm, respectively; (b) TEM, scale bar 500 nm, and (c) 3D surface profile plot with layer histograms of the selected area of the TEM image (red square) highlighting the layered appearance of Ind-CPP; (d–f) schematic interlocked Lego-type representation of the stacked Ind-CPP sheets along with the intra- and inter-molecular hydrogen bonding interactions; (g) deconvoluted FT-IR pattern of C═O and aromatic C═C (left), and N–H (right) stretching in Ind-CPP.

and 3.129 Å for the intra- and inter-planar interactions respectively in HBD_{112}, and 2.234 Å for the intraplanar interaction in HBD_{11}. Evidently, the C═O bond length in the first case is higher than that in the second one ($C═O_{112}$ 1.208 *vs.* $C═O_{11}$ 1.159 Å). This changes the average aromatic C–C bond length as well from 1.33 Å in the HBD_{112} case to 1.37 for the latter, whereas the $N–H_{112}$ length is 1.044 Å compared to 0.944 Å for $N–H_{11}$. The FTIR spectra of the polymer provided experimental validation to this theoretical calculation manifesting distinct C═O and aromatic C–C stretching bands originating from HBD_{112} and HBD_{11} interactions (Fig. 1g). On the other hand, the H–N stretching band can be deconvoluted into two peaks, also arising from these interactions (Fig. 1g).[32,33] The position of these IR peaks is a direct consequence of the length and order of these bonds, where stronger bonds (*i.e.*, shorter bond length) appeared at higher energy (Discussion S5†).

The UV-Vis spectra recorded for Ind-CPP demonstrate a significant redshift of the peaks compared to Tyrian purple (Fig. S10†). The n–π* peaks originating from the H-bonding bay sites showed 53 and 46 nm redshifts, while the π–π* band shifted by 31 nm towards a higher wavelength. In line with solid-state NMR, FTIR and XRD, this observation infers a high degree of polymerization. Effective Sonogashira polymerization increases the overall conjugation of the CPP skeleton initiating a redshift in absorption peaks. It is due to this augmented absorption pattern that the Ind-CPP polymer appeared as a deep bottle-green solid, whereas its monomer Tyrian purple is blue/purple.

A typical type-II N_2 sorption isotherm was recorded for the material at 77 K to assess the surface area and porosity. The sharp rise of the curve in the low relative pressure region inferred the presence of substantial micropores in the polymer network, whereas the wide hysteresis accounts for its mesopore content (Fig. S11†). This dual porosity was further confirmed by the non-local density functional theory (NLDFT) porosity pattern with two apexes at *ca.* 1.0 and 2.1 nm (Fig. S11†). Ind-CPP possessed 0.22 $cm^3\ g^{-1}$ total pore volume, of which mesopores contribute 86%. This extensive mesopore concentration can be perceived from the NLDFT plot as well. A rich mesopore content usually indicates a relatively low Brunauer–Emmett–Teller (BET) surface area. This was indeed the case of Ind-CPP featuring a BET surface area of 270 $m^2\ g^{-1}$.

As an auxiliary proof for the network structure of Ind-CPP, we also conducted thermogravimetric analysis (TGA) of the material (Fig. S12†). After activating Ind-CPP at 120 °C under vacuum for 12 h, the TGA curve shows a 7% weight loss at around 100 °C temperature indicating the loss of trapped water. A further *ca.* 27% weight loss was observed at 300 °C suggesting the collapse of the network structure.

Electrochemical impedance spectroscopy (EIS) of Ind-CPP conducted separately under no-bias in phosphate buffer solution (PBS, pH 7), 0.5 M aqueous H_2SO_4 (pH 0), and 1 M KOH (pH 14) demonstrated distinctive features. The Nyquist plots for all three cases fit perfectly to the Randle-type equivalent circuit given in Fig. 2a.[39–42] A massive drop in electrochemical impedance can be recorded for Ind-CPP in an acidic medium compared to the neutral medium, which is again slightly lower than that under alkaline conditions. Circuit breakdown analysis confirmed a cumulative contribution from series resistance (R_S), charge transfer resistance (R_{CT}), and Warburg impedance (Z_W) to the total electrochemical impedance of the CPP. As indicated in the impedance table (Fig. 2c), the R_S was least under acidic conditions, which increased with escalating pH. Since R_S is associated with the resistance of the medium, and the excess availability of free ions in the acidic and alkaline media compared to the neutral PBS can be the reason behind this drive. The R_{CT} of the material also manifested a pH-dependent trend. The measured R_{CT} value dropped by *ca.* 10% going down from pH 14 to pH 7, which consequently decreased further by a massive 94% at pH 0. An identical trend was followed by Z_W as well with a successive 12% and a further 94% drop in impedance going from pH 14 to 7 to pH 0.

The R_{CT} drives the charge transfer at the electrode–electrolyte interface. A huge decrease in these values indicates evident structural modification upon pH switching,[39–42] a phenomenon that can be explained considering the bay H-shift isomerization in indigo (Fig. 2d).[31–33] Upon excitation, indigo moieties manifest a 1,5-H shift in the bay position from amine N to carbonyl O. The presence of protons up-thrusts this transformation generating a cationic unit. We reckon an identical incident at lower pH, providing a holistic multi-cationic backbone of Ind-CPP. As the mono-H transferred derivative is marginally higher in energy than the pristine indigo, the CPP can't experience this structural shift in a neutral or alkaline medium, unless excited.[43] Due to the generation of multi-ionic sites, the electronic transport through the material becomes easier resulting in the abrupt lowering of R_{CT} values in an acidic medium. The change in pH and the presence of ionic sites at the electrode surface additionally mandate the electrical double layer to behave differently with a non-equilibrium charge and mass diffusion from the bulk. This contrives the contribution from Warburg's impedance.

As an experimental validation of the bay H-shift in Ind-CPP, we subjected the material to X-ray photoelectron spectroscopy (XPS) analysis. The high-energy photoelectron beam shot at Ind-CPP during XPS analysis was expected to make the material energetically excited, resulting in structure-specific bands originating from the mono-H-shifted derivative. As depicted in Fig. 2b, the N 1s HR-XPS region can be deconvoluted into three bands originating from N–H, N–C, and N=C of the H-transferred Ind-CPP. Similarly, the O 1s HR-XPS region can also be deconvoluted into four bands, one from the carbonyl, one from the O–H of the H-shifted material, and the other two are due to the surface adsorbed O_2 and water from the atmosphere through H-bonding. On the other hand, the HR-XPS spectra of the C 1s region were recorded and deconvoluted as well to provide an auxiliary justification of the chemical structure and functionalities of Ind-CPP (Fig. S13, Discussion S6†).

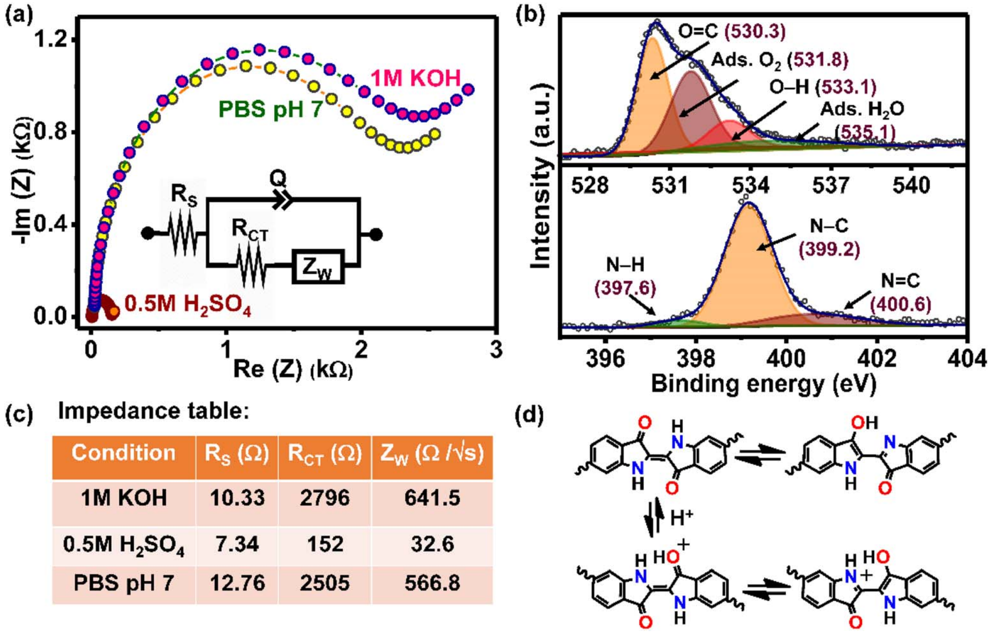

(c) Impedance table:

Condition	R_S (Ω)	R_{CT} (Ω)	Z_W (Ω /√s)
1M KOH	10.33	2796	641.5
0.5M H_2SO_4	7.34	152	32.6
PBS pH 7	12.76	2505	566.8

Fig. 2 (a) The EIS pattern of Ind-CPP at variable pH along with the Randle-type equivalent circuit and (c) corresponding data table; (b) deconvoluted O1s and N1s HR-XPS pattern of Ind-CPP; (d) pH-induced 1,5-bay H-shift in Ind.

2.2. Electrocatalytic activity

A standard three-electrode system was employed for the electrochemical HER experiments with Ind-CPP drop-cast on a glassy carbon electrode as the working electrode.[44,45] The material was envisaged to perform better under acidic conditions due to its favourable impedance behaviour. The *iR*-compensated current density (j) *vs.* potential (V) curve presented in Fig. 3a asserts this activity. In an acidic medium, Ind-CPP manifested an overpotential (η) of 359 mV at 10 mA cm^{-2} current density (η_{10}), whereas in an alkaline medium, 364 mV η_{10} was calculated. A comparison of these η-values inferred that Ind-CPP requires comparatively lower potential at pH 0 than at pH 14 (Fig. S14†). However, the difference between the catalytic activities of the polymer in different media ($\Delta\eta$) can be better perceived at a higher current density. The material shows almost no tangible catalytic disparity at η_{10}, while at j = 100 mA cm^{-2}, $\Delta\eta > 5$ units can be perceived. This behaviour is reflected in the j–V curve and corresponding Tafel slopes. The polarization curves drifted significantly apart from each other at higher η in acidic and alkaline media (Fig. 3a). Accordingly, a Tafel slope of 64 mV dec^{-1} was calculated for Ind-CPP at pH 0, which increases to 73 mV dec^{-1} at pH 14 further suggesting higher activity of the material in the acidic medium (Fig. 3b).

The HER mechanism, in general, can be pinned down to a combination of three individual pathways: Volmer, Heyrovsky, and Tafel, which are given as follows:[17]

(i) Adsorption of H in the catalyst given by the Volmer equation ($H^+ + e^- \rightarrow H_{ads}$ in an acidic and $H_2O + e^- \rightarrow H_{ads} + HO^-$ in an alkaline medium)

(ii) Desorption of H_2 following the Heyrovsky pathway ($H_{ads} + H^+ + e^- \rightarrow H_2$ in an acidic and $H_{ads} + H_2O + e^- \rightarrow H_2 + HO^-$ in an alkaline medium)

(iii) Desorption of H_2 following the Tafel pathway ($H_{ads} + H_{ads} \rightarrow H_2$, pH-independent)

The Volmer step dealing with H-adsorption *via* electron transfer is the initial step of the HER and is common for all materials, whereas the desorption of H_2 goes either *via* the Heyrovsky step consisting of electron transfer or following the Tafel pathway as physical desorption. The value of the Tafel slope empirically dictates the rate-determining step for the HER: 30 mV dec^{-1} suggests that the Tafel step is the rate-determining step, whereas 40 and 120 mV dec^{-1} respectively signify Heyrovsky and Volmer as the slowest step.[46] Despite the well-conferred existence of these proposed routes for metal-based catalysts involving metal–H bonds, whether a metal-free material can exhibit similar catalytic behaviour is still unknown.[45] We reckon that crafting the organic network with indigo can enable these processes by exploiting its redox properties and H-bonding site-mediated protonation–deprotonation activities. With this, we can affirm that the Heyrovsky step is the HER rate-determining step in our case, *i.e.*, the reaction is preferentially following a Volmer–Heyrovsky pathway.

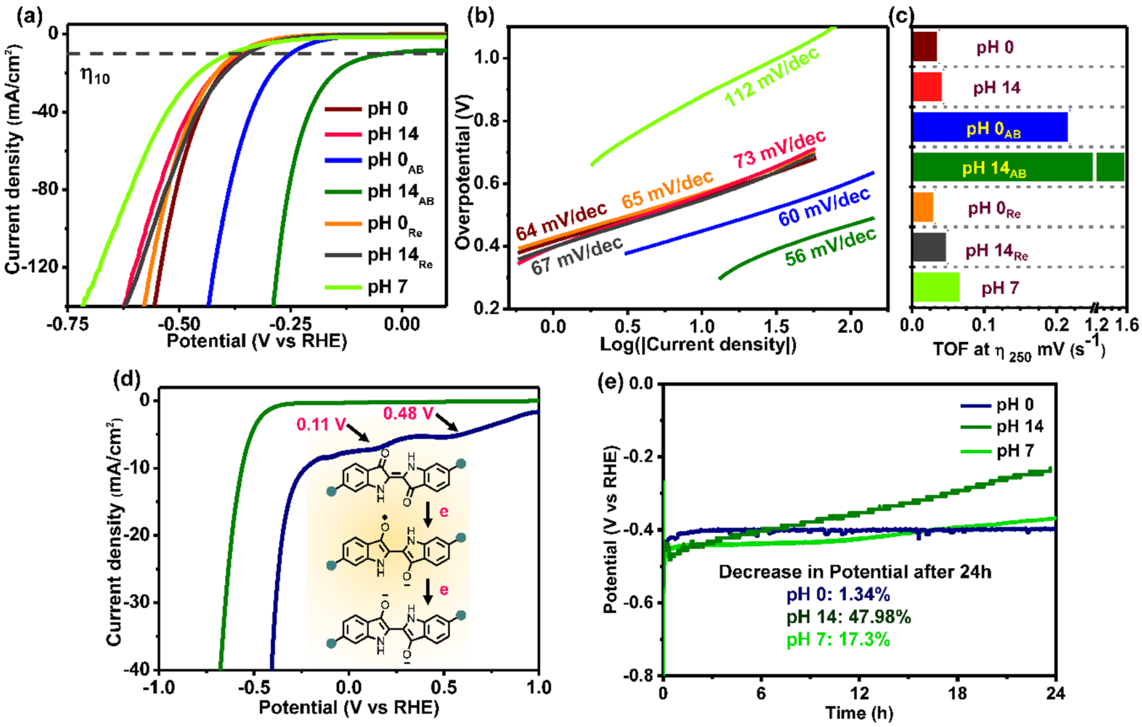

Fig. 3 (a) Polarization curves of Ind-CPP under various conditions and (b) the Tafel slopes corresponding to the polarization curves recorded in (a); (c) H_2 turnover frequency calculated at 250 mV η for Ind-CPP under various conditions corresponding to the polarization curves given in (a); (d) comparison of the polarization curves at pH 14 for fresh Ind-CPP and after bulk HER along with the *in situ* reduction of CPP (inset) showing reduction potentials; (e) bulk HER activity of Ind-CPP at a constant 10 mA cm^{-2} current density (chronopotentiometry).

Intrigued by the almost equipotent activity of the material at two extreme pHs, we further sought its activity in a neutral medium (PBS, pH 7). A truly pH-universal HER catalyst is particularly beneficial for practical purposes as one can use acidic, alkaline, or even direct seawater, effectively simplifying the process and slashing the production costs. In a neutral medium, Ind-CPP manifested a tad slower activity than in an acidic or alkaline medium (Fig. 3a). A *ca.* 20 mV higher η_{10} compared to pH 0 and 14 can be calculated from the polarization curve ($\eta_{10} = 384$ mV). The reaction proceeded at a relatively slower rate as indicated by the 112 mV dec^{-1} Tafel slope. Though the material still follows the Volmer–Heyrovsky route at neutral pH, the Volmer step appeared slower compared to the previous scenarios. Given the lack of catalytic ionization in a neutral medium, such a retarded reaction rate is justified.

Notably, most of the HER catalysts reported to date function only in an acidic medium, although there are examples of a handful of materials working effectively in an alkaline medium. A material demonstrating HER activity in a neutral medium is extremely rare, while pH-universal catalytic materials devoid of any metals are the rarest. To posit the HER activities of Ind-CPP with regard to other metal-free materials at different pH, a thorough comparison of individual catalytic activities has been made in terms of overpotential and Tafel slopes. Ind-CPP demonstrated either comparable or better HER capability than other metal-free systems reported to date (Fig. S15, Table S2, Discussion S7†).

The cyclic voltammogram (CV) of Ind-CPP recorded in acetonitrile for the assessment of its reduction potentials revealed that the polymer network possesses a conduction band edge at −0.56 V (*vs.* Ag/AgNO$_3$) (Fig. S16†). The CV curve of Ind-CPP further highlights the presence of another secondary reduction apex with an edge potential of −0.03 V (*vs.* Ag/AgNO$_3$). This is in agreement with the pH-independent two-electron reduction of indigo to its bis-anionic leuco analogue, Ind^{2-} (Fig. 5). To translate this observation into the catalytic HER context, we further conducted LSV measurements of Ind-CPP in aqueous PBS (pH 7) (Fig. S17†). Here we can also see two distinct reduction peaks at 0.03 V and 0.12 V (*vs.* RHE), much before the reduction potential of the HER. The water reduction starts only after the second reduction at 0.12 V. This, *ipso facto*, surmises that Ind-CPP will itself get reduced to Ind^{2-} before it starts reducing water to H$_2$ within its reduction potential window. To further confirm this, we derived a Tafel-slope-inspired log(current density) *vs.* potential (*vs.* RHE) curve from this LSV, which gave three different slopes (Fig. S17†). This qualitatively justifies the two-electron indigo reduction followed by the HER. The Ind^{2-} can uptake one or two proton(s) from the medium facilitating the Volmer step of the HER (Fig. 5). The excess availability of H$^+$ under acidic conditions causes faster proton abstraction than in an alkaline or neutral medium, where water acts as the proton source for Ind^{2-}. Evidently, Ind-CPP manifests better catalytic activity at pH 0.

Following this, the stability of the electrode was assessed at a constant 10 mA cm^{-2} current density for 24 h at two extreme pH values. We expected better catalytic performance of Ind-CPP in an acidic medium as already comprehended from the polarization curves, which was indeed the case for the initial few hours of the bulk HER. However, with passing time, the catalytic activity at pH 14 gradually increases, and at the end of 24 h span, an almost 48% decrease in the required potential was observed compared to only a 1.34% decrease in the potential requirement for pH 0 (Fig. 3e). A similar trend was observed at pH 7 as well with a 17% potential drop after 24 h. Of note, the potential requirement dropped in all cases suggesting that irrespective of the pH of the medium, the catalytic activity of Ind-CPP successively increased during the bulk HER, though the effect is more pronounced in an alkaline medium. The polarization curves recorded after bulk HER demonstrated surprisingly superior activity to that under the pristine conditions with a reversal in the medium-dependent activity (AB, Fig. 3a). As depicted in Fig. 3a, Ind-CPP possessed a substantial decline in η after bulk HER at both pH, while the decrease is much profound at pH 14. Specifically, η_{10} values of 249 and 28 mV were recorded for Ind-CPP at pH 0$_{\text{AB}}$ and 14$_{\text{AB}}$, respectively compared to 359 and 364 mV, *i.e.*, η_{10} dropped by *ca.* 30% and 92% at pH 0 and 14, respectively. This apparent anomaly can be justified considering the previously discussed reduction of Ind to Ind^{2-}. As the reaction progresses, simply more amounts of CPP were reduced. In the alkaline medium, these newly augmented anionic motifs retained their ionic character amplifying the water–catalyst contact, whereas, in the acidic medium, the material mostly acquired a corresponding alcohol backbone (*i.e.*, IndH$_2$). Though these structural alterations enhanced the catalytic propensity of the pristine network, in either case, the ionic backbone of the CPP in an alkaline medium accounts for its superior activity (Fig. 5).

A comparison of the polarization curves at pH 14, recorded before and after bulk HER in an extended positive potential range, demonstrates that the CPP material possessed two clear reduction peaks before it starts catalysing the HER (Fig. 3d). The edge potentials of these two peaks are the same as the reduction edge of Ind-CPP observed in the CV and LSV experiments (Fig. S17†), indicating the presence of reduced leuco-Ind-CPP on the electrode. However, no such peaks can be perceived for the pristine Ind-CPP. This, in turn, endorses the *in situ* reduction of Ind to leuco-Ind during the HER, and that the reduced moiety is responsible for the better catalytic performance of the material. In line with this, the contribution from Warburg impedance in the EIS pattern of the polymer further indicated the presence of a non-equilibrium charge/mass transfer process involved at the electrode–electrolyte interface and the double layer; more specifically a proton-coupled electron transfer process.[47–50]

For further experimental corroboration of this catalyst-reduction-induced HER performance of Ind-CPP, we performed a series of impedance analyses of the material at pH 14 (1 M KOH aq.) under potentiostatic conditions. Seven sequential potentials were chosen as independent biases in the 0.7 V to 0.1 V (*vs.* RHE) range to monitor the changes in R_{CT}, R_{bulk}, and phase angles of Ind-CPP during its reduction. A massive impedance of the material was recorded at 0.7 V (Fig. 4a). The spectra can be fitted to an equivalent Randle circuit $[R_{\text{S}} + (Q_{\text{bulk}}/R_{\text{bulk}}) + (C_{\text{CT}}/(R_{\text{CT}} + W))]$ (Fig. 4b). This agrees with the previous EIS conducted under zero bias showing significant Warburg contribution, which in turn, indicates the capacitive nature of the material at this potential.

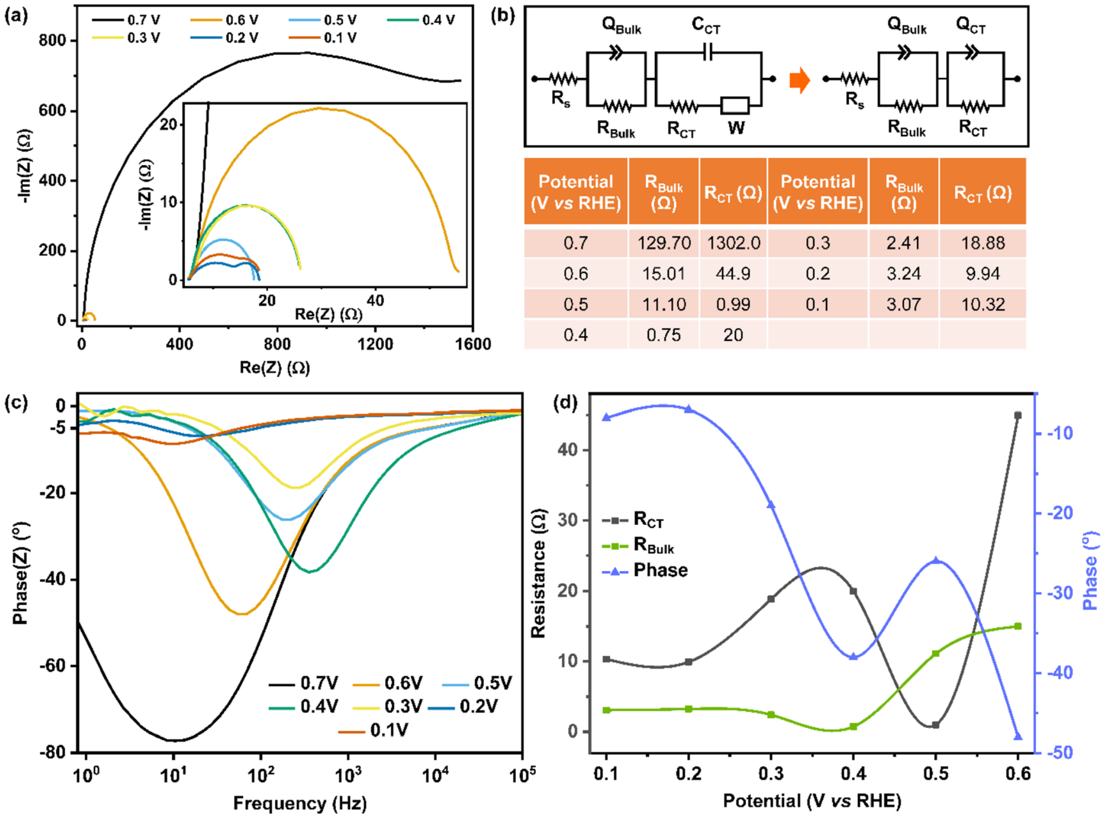

Potential (V *vs* RHE)	R_{Bulk} (Ω)	R_{CT} (Ω)	Potential (V *vs* RHE)	R_{Bulk} (Ω)	R_{CT} (Ω)
0.7	129.70	1302.0	0.3	2.41	18.88
0.6	15.01	44.9	0.2	3.24	9.94
0.5	11.10	0.99	0.1	3.07	10.32
0.4	0.75	20			

Fig. 4 (a) The Nyquist plots of Ind-CPP in 1 M aqueous KOH at different potentials showing the massive drop in impedance with lowering bias potentials (inset), and (b) corresponding Randle circuits with resistance values, and (c) Bode plots. (d) The change in bulk and charge-transfer resistance, and phase angle of Ind-CPP at different potentials showing stepwise reduction of the material and corresponding change in the double-layer.

The corresponding Bode plot (Fig. 4c) also justifies this high capacitive nature of Ind-CPP at 0.7 V. Considering the CV of the material (Fig. 3d, inset and S16†), it can be understood that it is still within the non-faradaic zone, which signifies such a high capacitive current. Going down from 0.7 to 0.6 V, the impedance massively dropped with a change in the Randle circuit pattern to [R_S + (Q_{bulk}/R_{bulk}) + (Q_{CT}/R_{CT})], which remained a good fit for the Nyquist plots derived from EIS measurements at the subsequent potentials as well (*cf.* Fig. 4a inset and 4b). Gradually changing the bias potential from 0.6 V to 0.1 V presented interesting R_{CT}, R_{bulk}, and phase angle trends (Fig. 4d). R_{bulk} gradually decreased with decreasing potential till 0.4 V and then remained almost constant suggesting no significant change in the bulk electronic conduction of Ind-CPP at lower biases. On the other hand, the R_{CT} significantly dropped as we changed the bias from 0.6 V to 0.5 V, and then increased again at 0.4 V before dropping again to become almost constant at 0.2 V (Fig. 4a inset, 4b and d). The Bode plots also show the significance of this potential range as the phase angles (and thereby the capacitive nature) complemented the R_{CT} trend, *i.e.*, it dropped going down from 0.6 V to 0.5 V before increasing again at 0.4 V and finally dropping and becoming almost constant at 0.2 V (Fig. 4c and d). This trend can be explained considering the CV of the material and the stepwise two-electron reduction of the Ind-moiety before it starts catalysing the HER. After the first reduction, Ind-CPP acquires an ionic structure resulting in a rapid change in the adjacent double layer, which in turn led to a low R_{CT} and decrease in the phase angle. On further lowering the potential, a new double-layer starts to form until the second reduction of Ind. This can explain the intermittent increase in R_{CT} and the capacitive nature of the material before its final drop. As it gets fully reduced, no significant changes in these values can be observed from then on, indicating the sole presence of a catalytic current.

The double-layer capacitance (C_{dl}) of the material was calculated in 0.5 M H_2SO_4 from the non-faradic region of its cyclic voltammogram recorded at varied scan rates (Fig. S18†). At low scan rates (till 200 mV s^{-1}) 145.6 μF cm^{-2} C_{dl} can be calculated which decreased to 80.0 μF cm^{-2} at higher scan rates (till 1 V s^{-1}). Owing to the redox activity of Ind-CPP during the HER, the extent of electrode–electrolyte interfacial electrochemical reactions tends to cease with increasing scan rate leading to a decreased C_{dl}. The current density-dependent turnover frequency (TOF) for H_2 production *vis-à-vis* amount per unit time was calculated from the electrochemical surface area of Ind-CPP as a quantifiable measure of its catalytic activity (Discussion S8†). After normalizing against the active catalytic sites *i.e.*, the indigo cores, the material was found to manifest a TOF of 1.58 H_2 per s at 250 mV η after bulk electrolysis at pH 14 (Fig. 3c, Discussion S8†). This is equivalent to *ca.* 1.53 kg H_2 per 1 g of Ind-CPP produced from water every day (Discussion S8†).

2.3. Mechanism

We sought theoretical explanations to better justify our experimental findings and the corresponding discussions. Accordingly, using 6,6′-bis(phenylethynyl)indigo (Ind-Mod, Fig. S19†) as a theoretical model for the Ind-CPP, all possible electrode–electrolyte interfacial scenarios including various Ind-reduced and H^+ abstracted structures, and their interactions with water/additional H^+ were computed through successive geometry and energy optimization using AM1 Hamiltonian with restricted Hartree–Fock in the VAMP module of Biovia Materials Studio. Depending on the pH of the reaction medium, different Volmer and Heyrovsky pathways were proposed (Fig. 5) and the

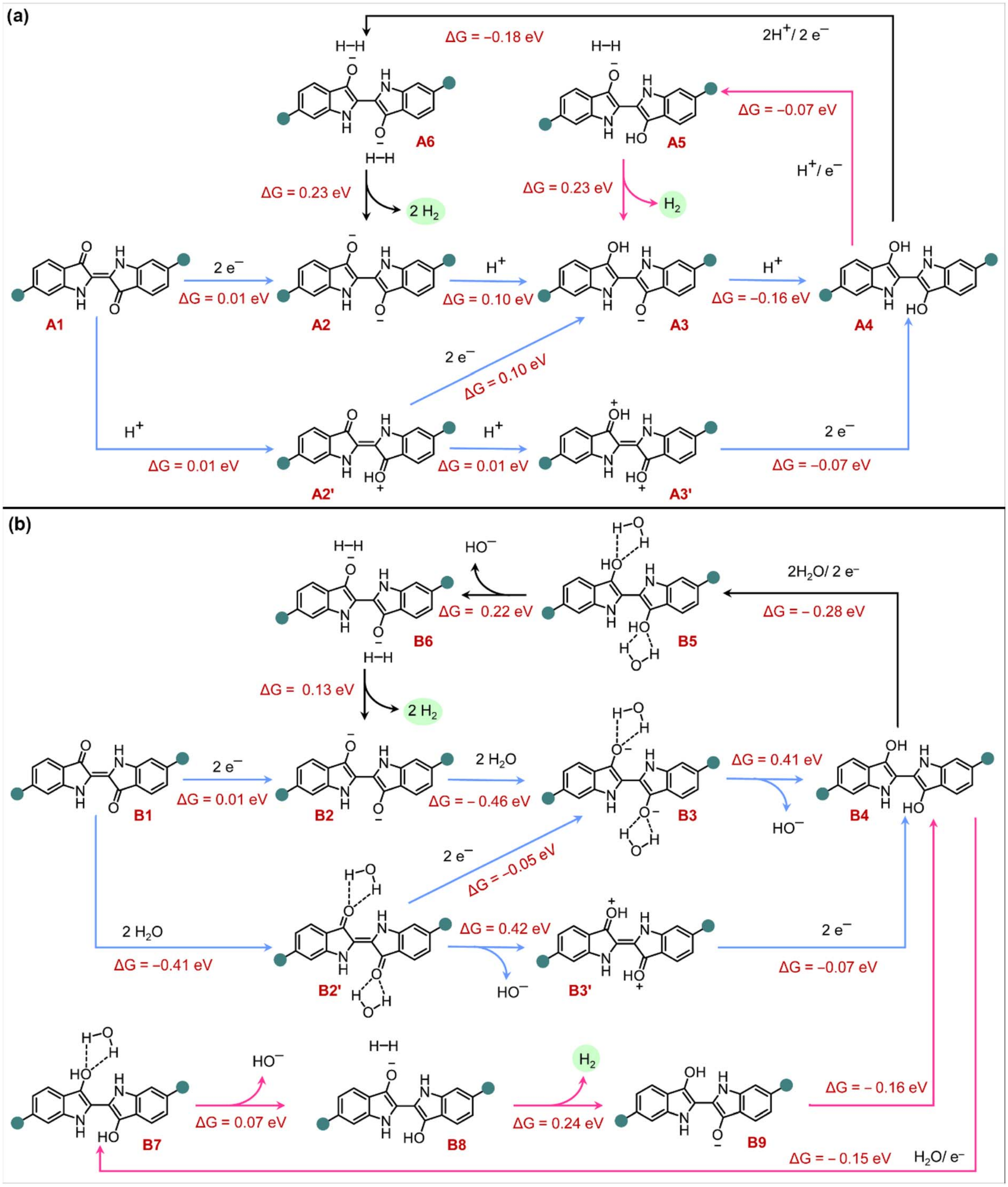

Fig. 5 Mechanistic diagram of the proposed Volmer–Heyrovsky pathway of the HER with the corresponding free-energy change at (a) pH 0 and (b) pH 7 and 14. The Volmer route is indicated by the blue arrows, whereas the Heyrovsky steps are shown by pink (one-electron shunt) and black (two-electron shunt) arrows.

changes in free energy, ΔG (eV), for each of these intermediates (reactants/products) involved in the two pathways were estimated. The Volmer steps are shown by blue arrows, whereas the Heyrovsky paths are shown by pink (one-electron shunt) and black (two-electron shunt) arrows. The optimized structures of all possible intermediates, reactants, and products along with their structural details can be found in the ESI (Table S4†).

The HER pathway in an acidic medium is shown in Fig. 5a, whereas those for pH 7 and 14 are given in Fig. 5b. The figure clarifies that the Volmer route (blue arrows) to H-adsorption can be deconstructed into two steps: (i) association of the material with water (or protons) and (ii) its reduction. The pristine Ind-Mod (**A1** or **B1** in Fig. 5) can generate the Volmer product **A4** (or **B4**) either by step (i) followed by step (ii), or *vice versa*. The small magnitude of ΔG values suggests that both routes are feasible to obtain the Volmer product.

There is no further scope for the direct reduction of the Volmer product (*i.e.*, **A4** or **B4**) within our working potential window. This substantiates that the only possible protocol of the Heyrovsky mechanism is protonation (or water association) of this Volmer product followed by reduction and H_2 generation. As portrayed in Fig. 5, the Heyrovsky route can be achieved either through single protonation and a one-electron shunt generating one equivalent of H_2 (pink arrow) or by a concerted bis-protonation and two-electron shunt producing two equivalents of H_2. Though both these steps are energetically favourable, the overall ΔG of the Heyrovsky route is slightly higher than the Volmer step, resulting in a slower speed of the former. This was indeed validated by the experimental Tafel slopes of the material, where Heyrovsky was regarded as the rate-determining step (*vide supra*). Moreover, the calculated free energy values for the overall HER reactions range from −0.06 eV to 0.12 eV depending on the different catalytic pathways, where the two-electron shunt offered energetically more favourable routes under both acidic and alkaline conditions. Regardless, the low ΔG values justify the faster reaction rates, and *ergo* low Tafel slopes.

One particularly interesting observation is that the ΔG of the water-association steps (**B2′**, **B3**, **B5**, and **B7**) is sufficiently lower compared to the following dissociation of the OH^-. The exact energy values recorded in Tables S4 and S5† show a *ca.* −0.15 to −0.46 eV drop in energy after hydration. The structural evaluation of these compounds revealed that the water molecules are oriented around the Ind-core in a way to experience maximum H-bonding interactions (Fig. 5, 6 and Table S5†). The leuco analogue **B5** and **B7** show three-fold H-bonding attractions with the C–OH of Ind at bay positions, whereas **B3** and **B2′** have multi-fold H-bonding with the bay C=O and N–H. It can be observed that B3 manifested the strongest association with water due to its ionic nature, and consequently, possessed the lowest free energy compared to the other intermediates.

To experimentally corroborate the CPP–water H-bonding association during catalysis, the catalysts (from pH 0, 7, and

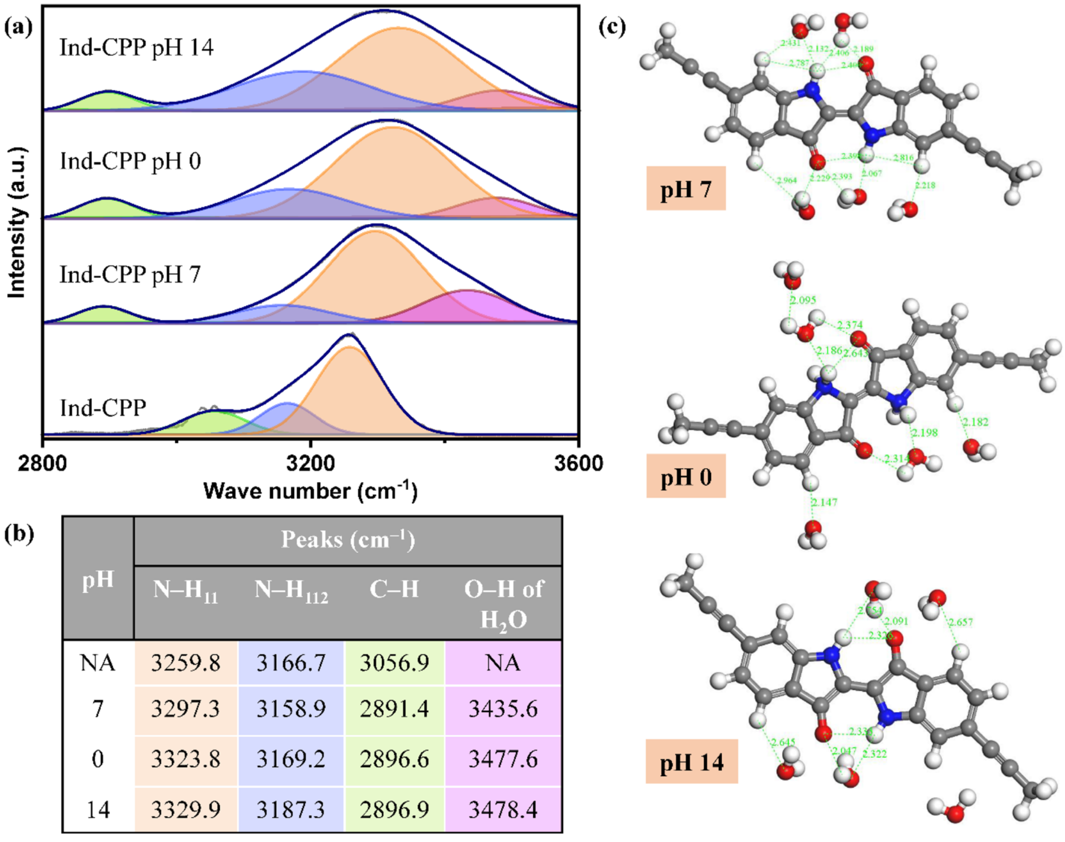

pH	Peaks (cm^{-1})			
	N–H_{11}	N–H_{112}	C–H	O–H of H_2O
NA	3259.8	3166.7	3056.9	NA
7	3297.3	3158.9	2891.4	3435.6
0	3323.8	3169.2	2896.6	3477.6
14	3329.9	3187.3	2896.9	3478.4

Fig. 6 (a) Deconvoluted FTIR peaks in the 2800–3600 cm^{-1} range showing the change in Ind-CPP after its association with water during catalysis with (b) the corresponding peak positions and (c) theoretical models.

14) were scraped off the GCE surface after a 12 h HER run, dried at 120 °C, and subjected to FTIR analysis. As shown in Fig. 6a, compared to the pristine Ind-CPP, all three used materials show a distinct spectral pattern in terms of peak positions. While the N–H_{112} peaks arising from interplanar interactions remain almost unchanged, the N–H_{11} peaks undergo blueshift. Moreover, a new peak emerges at ~3430–3470 cm^{-1} from the trapped water (even after high-temperature drying). On the other hand, the aromatic C–H bands show a prominent redshift. These observations jointly suggest the existence of the H-bonding interaction of the Ind-unit with water during catalysis (Fig. 6b).[51–56] A simulated model of Ind–water interaction at different pH (0, 7, and 14) further provides theoretical justification for the existing interaction of water with N–H and aromatic C–H units corroborating the experimental FTIR analysis (Fig. 6c).

As with each catalytic run, Ind-CPP will convert to its reduced form, *i.e.*, the intermediate for the Volmer step, and the amounts of the Volmer intermediate start piling up leading to better HER catalytic activity. We reckon that the chemical structure of Ind^{2-} is identical to the intermediate generated during the production of the blue dye from indoxyls. Therefore, the pristine Ind-CPP can be regenerated *post operando* simply by storing the working electrode in air.[57] Accordingly, after bulk HER the Ind-CPP electrode kept in the air atmosphere for 1 week offered almost identical polarization curves and Tafel slopes to the parent material (Re, Fig. 3a and b).

3. Conclusion

In conclusion, we have introduced an indigo-based organic conjugated porous polymer as a metal-free pH-universal catalyst for electrochemical H_2 production from water. Due to the H-bonding interactions between indigo molecules, the resultant polymer appeared with a 2D lamellar morphology with micrometre-sized sheets stacked on each other. After exfoliation *via* sonolysis, these sheets provided multiple H-bonding sites that were initially engaged in inter-planar interactions. These newly available H-bonding sites manifested augmented water (and proton)-attraction facilitating the Volmer step of the HER. We have utilized the vat-dye properties of the indigo structure, *i.e.*, its reduction to the di-anionic leuco form *in situ* during catalytic assay to enhance the electrochemical behaviour of the overall material. The fresh material performed better in the acidic medium over the alkaline and neutral medium in the initial course of the catalysis. However, the activity in the alkaline medium gradually increased over time due to the formation of an anionic leuco structure in the catalytic body resulting in enhanced electronic conduction. The Tafel slope calculated from experimental polarization curves indicated a Volmer–Heyrovsky-type mechanism, which was further endorsed by the theoretically calculated energy diagram of the reactants, intermediates, and products.

Conflicts of interest

There are no conflicts to declare.

Acknowledgements

The authors acknowledge the financial contribution of the Wuhan University of Technology. I. N. and J. C. acknowledge the Chinese Postdoctoral Fellowship.

References

1 J. A. Turner, *Science*, 2004, **305**, 972–974.
2 M. G. Walter, E. L. Warren, J. R. McKone, S. W. Boettcher, Q. Mi, E. A. Santori and N. S. Lewis, *Chem. Rev.*, 2010, **110**, 6446–6473.
3 V. Artero, M. Chavarot-Kerlidou and M. Fontecave, *Angew. Chem., Int. Ed.*, 2011, **50**, 7238–7266.
4 S. Cobo, J. Heidkamp, P.-A. Jacques, J. Fize, V. Fourmond, L. Guetaz, B. Jousselme, V. Ivanova, H. Dau, S. Palacin, M. Fontecave and V. Artero, *Nat. Mater.*, 2012, **11**, 802–807.
5 P. Du and R. Eisenberg, *Energy Environ. Sci.*, 2012, **5**, 6012–6021.
6 T. F. Jaramillo, K. P. Jørgensen, J. Bonde, J. H. Nielsen, S. Horch and I. Chorkendorff, *Science*, 2007, **317**, 100–102.
7 R. Subbaraman, D. Tripkovic, D. Strmcnik, K.-C. Chang, M. Uchimura, A. P. Paulikas, V. Stamenkovic and N. M. Markovic, *Science*, 2011, **334**, 1256–1260.
8 J. Kibsgaard, Z. Chen, B. N. Reinecke and T. F. Jaramillo, *Nat. Mater.*, 2012, **11**, 963–969.
9 D. Voiry, H. Yamaguchi, J. Li, R. Silva, D. C. B. Alves, T. Fujita, M. Chen, T. Asefa, V. B. Shenoy, G. Eda and M. Chhowalla, *Nat. Mater.*, 2013, **12**, 850–855.
10 S. Najmaei, Z. Liu, W. Zhou, X. Zou, G. Shi, S. Lei, B. I. Yakobson, J.-C. Idrobo, P. M. Ajayan and J. Lou, *Nat. Mater.*, 2013, **12**, 754–759.
11 A. B. Laursen, S. Kegnæs, S. Dahla and I. Chorkendorff, *Energy Environ. Sci.*, 2012, **5**, 5577–5591.
12 D. Merki and X. Hu, *Energy Environ. Sci.*, 2011, **4**, 3878–3888.
13 A. C. Johnson, X. Jin, N. Nakada and J. P. Sumpter, *Science*, 2020, **367**, 384–387.
14 K. Kümmerer, J. H. Clark and V. G. Zuin, *Science*, 2020, **367**, 369–370.
15 European Commission, *Implementation of the Circular Economy Action Plan*, 2019.
16 U.N. Environment Programme, *Global Chemicals Outlook II*, 2019.
17 R. Subbaraman, D. Tripkovic, K.-C. Chang, D. Strmcnik, A. P. Paulikas, P. Hirunsit, M. Chan, J. Greeley, V. Stamenkovic and N. M. Markovic, *Nat. Mater.*, 2012, **11**, 550–557.
18 X. Wang, K. Maeda, A. Thomas, K. Takanabe, G. Xin, J. M. Carlsson, K. Domen and M. Antonietti, *Nat. Mater.*, 2009, **8**, 76–80.
19 Y. Wang, A. Vogel, M. Sachs, R. S. Sprick, L. Wilbraham, S. J. A. Moniz, R. Godin, M. A. Zwijnenburg, J. R. Durrant, A. I. Cooper and L. Tang, *Nat. Energy*, 2019, **4**, 746–760.
20 E. Jin, Z. Lan, Q. Jiang, K. Geng, G. Li, X. Wang and D. Jiang, *Chem*, 2019, **5**, 1632–1647.
21 J. Chakraborty, I. Nath, S. Song, S. Mohamed, A. Khan, P. M. Heynderickx and F. Verpoort, *J. Photochem. Photobiol., C*, 2019, **41**, 100319.

22 F. Vilela, K. Zhang and M. Antonietti, *Energy Environ. Sci.*, 2012, **5**, 7819–7832.

23 A. I. Cooper, *Adv. Mater.*, 2009, **21**, 1291–1295.

24 Y. Xu, S. Jin, H. Xu, A. Nagai and D. Jiang, *Chem. Soc. Rev.*, 2013, **42**, 8012–8031.

25 K. Mudiyanselage, S. D. Senanayake, L. Feria, S. Kundu, A. E. Baber, J. Graciani, A. B. Vidal, S. Agnoli, J. Evans, R. Chang, S. Axnanda, Z. Liu, J. F. Sanz, P. Liu, J. A. Rodriguez and D. J. Stacchiola, *Angew. Chem., Int. Ed.*, 2013, **52**, 5101–5105.

26 J. A. Rodriguez, S. Ma, P. Liu, J. Hrbek, J. Evans and M. Pérez, *Science*, 2007, **318**, 1757–1760.

27 H. Yin, S. Zhao, K. Zhao, A. Muqsit, H. Tang, L. Chang, H. Zhao, Y. Gao and Z. Tang, *Nat. Commun.*, 2015, **6**, 6430.

28 C.-T. Dinh, A. Jain, F. P. García de Arquer, P. De Luna, J. Li, N. Wang, X. Zheng, J. Cai, B. Z. Gregory, O. Voznyy, B. Zhang, M. Liu, D. Sinton, E. J. Crumlin and E. H. Sargent, *Nat. Energy*, 2019, **4**, 107–114.

29 J. C. Splitstoser, T. D. Dillehay, J. Wouters and A. Claro, *Sci. Adv.*, 2016, **2**, e1501623.

30 H. V. Olphen, *Science*, 1966, **154**, 645–646.

31 M. Irimia-Vladu, Y. Kanbur, F. Camaioni, M. E. Coppola, C. Yumusak, C. V. Irimia, A. Vlad, A. Operamolla, G. M. Farinola, G. P. Suranna, N. González-Benitez, M. C. Molina, L. F. Bautista, H. Langhals, B. Stadlober, E. D. Głowacki and N. S. Sariciftci, *Chem. Mater.*, 2019, **31**, 6315–6346.

32 X. He, F. Yang, S. Li, X. He, A. Yu, J. Chen, J. Xu and J. Wang, *J. Phys. Chem. A*, 2019, **123**, 6463–6471.

33 X. He, P. Yu, J. Zhao and J. Wang, *J. Phys. Chem. B*, 2017, **121**, 9411–9421.

34 W. Ai, W. Zhou, Z. Du, C. Sun, J. Yang, Y. Chen, Z. Sun, S. Feng, J. Zhao, X. Dong, W. Huang and T. Yu, *Adv. Funct. Mater.*, 2017, **27**, 1603603.

35 C. Yang, W. Huang, L. Caire da Silva, K. A. I. Zhang and X. Wang, *Chem.–Eur. J.*, 2018, **24**, 17454–17458.

36 J. Chakraborty, I. Nath and F. Verpoort, *Chem. Eng. J.*, 2019, **358**, 580–588.

37 H. Xu and K. S. Suslick, *J. Am. Chem. Soc.*, 2011, **133**, 9148–9151.

38 A. Jawaid, D. Nepal, K. Park, M. Jespersen, A. Qualley, P. Mirau, L. F. Drummy and R. A. Vaia, *Chem. Mater.*, 2016, **28**, 337–348.

39 Q. Han, Z. Cheng, B. Wang, H. Zhang and L. Qu, *ACS Nano*, 2018, **12**, 5221–5227.

40 B. Klahr, S. Gimenez, F. Fabregat-Santiago, J. Bisquert and T. W. Hamann, *J. Am. Chem. Soc.*, 2012, **134**, 16693–16700.

41 B. Klahr, S. Gimenez, F. Fabregat-Santiago, T. Hamann and J. Bisquert, *J. Am. Chem. Soc.*, 2012, **134**, 4294–4302.

42 O. Zandi and T. W. Hamann, *Nat. Chem.*, 2016, **8**, 778–783.

43 J. Pina, D. Sarmento, M. Accoto, P. L. Gentili, L. Vaccaro, A. Galvão and J. S. Seixas de Melo, *J. Phys. Chem. B*, 2017, **121**, 2308–2318.

44 Y. Yang, Y. Qian, H. Li, Z. Zhang, Y. Mu, D. Do, B. Zhou, J. Dong, W. Yan, Y. Qin, L. Fang, R. Feng, J. Zhou, P. Zhang, J. Dong, G. Yu, Y. Liu, X. Zhang and X. Fan, *Sci. Adv.*, 2020, **6**, eaba6586.

45 Y. Zheng, Y. Jiao, Y. Zhu, L. H. Li, Y. Han, Y. Chen, A. Du, M. Jaroniec and S. Z. Qiao, *Nat. Commun.*, 2014, **5**, 3783.

46 T. Shinagawa, A. T. Garcia-Esparza and K. Takanabe, *Sci. Rep.*, 2015, **5**, 13801.

47 Q. Hu, K. Gao, X. Wang, H. Zheng, J. Cao, L. Mi, Q. Huo, H. Yang, J. Liu and C. He, *Nat. Commun.*, 2022, **13**, 3958.

48 Q. Hu, Y. Qin, X. Wang, H. Zheng, K. Gao, H. Yang, P. Zhang, M. Shao and C. He, *CCS Chem.*, 2022, **4**, 2053–2064.

49 Q. Hu, Z. Wang, X. Huang, Y. Qin, H. Yang, X. Ren, Q. Zhang, J. Liu and C. He, *Energy Environ. Sci.*, 2020, **13**, 5097–5103.

50 Q. Hu, Z. Han, X. Wang, G. Li, Z. Wang, X. Huang, H. Yang, X. Ren, Q. Zhang, J. Liu and C. He, *Angew. Chem., Int. Ed.*, 2020, **59**, 19054–19059.

51 A. Melli, V. Barone and C. Puzzarini, *J. Phys. Chem. A*, 2021, **125**, 2989.

52 C. A. Hunter, *Angew. Chem., Int. Ed.*, 2004, **43**, 5310.

53 A. Halder, S. Karak, M. Addicoat, S. Bera, A. Chakraborty, S. H. Kunjattu, P. Pachfule, T. Heine and R. Banerjee, *Angew. Chem., Int. Ed.*, 2018, **57**, 5797.

54 A. Henao, A. J. Johnston, E. Guardia, S. E. McLain and L. C. Pardo, *Phys. Chem. Chem. Phys.*, 2016, **18**, 23006.

55 A. Bhattacherjee and S. Wategaonkar, *Phys. Chem. Chem. Phys.*, 2016, **18**, 27745.

56 S. Scheiner, T. Kar and J. Pattanayak, *J. Am. Chem. Soc.*, 2002, **124**, 13257.

57 C. Yi, X. Tan, B. Bie, H. Ma and H. Yi, *Sci. Rep.*, 2020, **10**, 4927.